

# The virtual ventricular wall: a tool for exploring cardiac propagation and arrhythmogenesis.

ARUN V. HOLDEN<sup>1</sup>, OLEG V. ASLANIDI<sup>1</sup>, ALAN P. BENSON<sup>1</sup>,  
RICHARD H. CLAYTON<sup>2</sup>, GRAEME HALLEY<sup>1</sup>, PAN LI<sup>1</sup> and  
WING CHIU TONG<sup>1</sup>

<sup>1</sup>*Computational Biology Laboratory, Institute of Membrane and Systems Biology,  
University of Leeds, Leeds LS2 9JT, UK*

<sup>2</sup>*Department of Computer Science, University of Sheffield, S1 4DP, Sheffield, UK*

**Abstract.** Methods for the experimental and clinical investigation of cardiac arrhythmias are limited to inferring propagation within the myocardium, from surface measurements, or from electrodes at a few sites within the cardiac wall. Biophysically and anatomically detailed computational models of cardiac tissues offer a powerful way for studying the electrical propagation processes and arrhythmias within the virtual heart. We use virtual tissues to study and visualise the effects of patho- and physiological conditions, and pharmacological interventions on transmural propagation in the virtual ventricular walls. Class III drug actions are quantitatively explained by changes induced in the transmural dispersion of action potential duration. We illustrate the automated construction of a virtual anisotropic ventricle from Diffusion Tensor MRI for individual hearts, and use it to explore mechanisms leading to ventricular fibrillation. The virtual ventricular wall provides an effective tool for exploring, evaluating and visualising processes during the initiation and maintenance of ventricular arrhythmias.

## 1. Introduction

Ventricular fibrillation (VF) is the most common cause of mortality from cardiovascular disease in the industrialised world. During VF rapid, self-sustained and spatio-temporally highly irregular electrical excitation waves in the ventricles results in loss of their normal contraction rhythm. Both experimental [1, 2, 3] and computational [4, 5] evidence supports the idea that VF is sustained by re-entrant wave propagation. There can be either a single re-entrant wave with fibrillatory conduction [6] or breakup of an initial re-entrant wave to multiple wavelets, due to cell restitution properties [7], effects of rotational anisotropy in the ventricular wall [8], or dynamic three-dimensional (3D) instabilities [9]: see Fig. 1.

Clinical studies of the mechanisms of ventricular fibrillation are limited, as the urgent necessity for treatment precludes more detailed investigations. Experimental studies are generally restricted to mapping electrical activity on the ventricular surfaces [7, 10, 11, 12], and major advances have been achieved through the simultaneous mapping

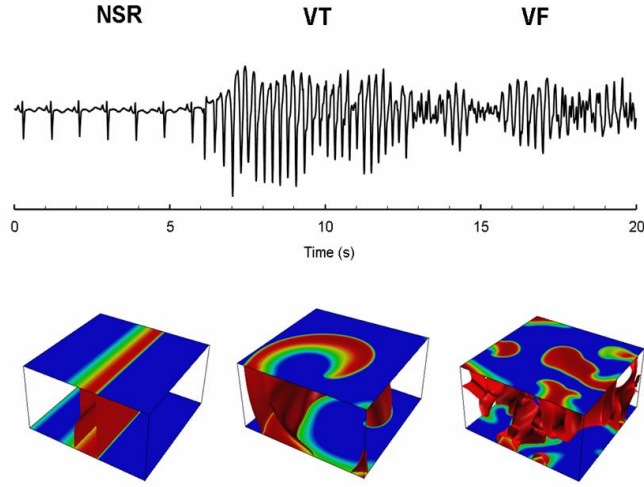


*Figure 1.* Schematic development of the electrogram of normal sinus rhythm (NSR) through ventricular tachycardia (VT) into ventricular fibrillation (VF), viewed as transition from transmural plane wave propagation, through an intramural scroll wave that breaks down into spatio-temporal irregularity.

of endocardial and epicardial activity in a ventricular slice preparation [6] and the panoramic mapping of activity over the surface of the entire heart [13, 14]. Theory, experiments and clinical studies all lead to a need to visualise, within the ventricular wall, the pattern of events occurring during VF.

Biophysically and anatomically detailed computational models of the ventricular wall – virtual ventricular tissues – provide a potentially powerful way to dissect, in time and space, the electrical excitation and propagation processes within the ventricles, and have been used to examine the 3D mechanisms that are consistent with experimental recordings of surface patterns during VF [7, 12, 15, 16, 17]. To succeed in providing insights into the initiation and control of ventricular arrhythmias, the models should combine a detailed biophysical description of the excitation kinetics of ventricular cells [18, 19], the spatial mapping of cell properties as membrane channel and inter-cellular coupling connexin expression maps [20] through the ventricles, and an accurate representation of the anisotropic geometry of the ventricular tissue, as in the Auckland canine model [21, 22].

In this paper we illustrate the construction of 1-, 2- and 3-dimensional virtual tissues and their application to study and visualise the effects

of patho- and physiological conditions, and pharmacological interventions on the propagation of excitation within in the ventricular walls. We account quantitatively for the pro-arrhythmogenic effects of two Class III anti-arrhythmic drugs by changes induced in the transmural dispersion of action potential duration. We illustrate the automated construction of the geometry and fibre orientation of the ventricles from Diffusion Tensor Magnetic Resonance Imaging of an individual heart, and use it to explore mechanisms leading to ventricular fibrillation. The virtual ventricular wall provides an effective tool for exploring, evaluating and visualising processes during the initiation and maintenance of ventricular arrhythmias.

## 2. Constructing virtual ventricular tissue

Virtual cardiac tissues have proved to be an effective tool for simulating cardiac propagation patterns, and for proposing hypotheses that can be tested experimentally [12, 17, 23, 24]. Propagation of electrical excitation in cardiac tissue can be described by the nonlinear partial differential equation [12, 15, 25]:

$$\frac{\partial V}{\partial t} = \nabla(D\nabla V) - I_{\text{ion}} . \quad (1)$$

Here  $V$  (mV) is the membrane potential,  $\nabla$  is a spatial gradient operator,  $t$  is time (ms).  $D$  is the diffusion coefficient tensor ( $\text{mm}^2/\text{ms}$ ), that characterises electrotonic spread of voltage.  $I_{\text{ion}}$  is the total membrane ionic current density. Cell membrane current densities are estimated in isolated cardiac cells by dividing the total cell current ( $\mu\text{A}$ ) by the total cell capacitance: on the assumption that this is predominantly the surface membrane capacitance, which for all cell membranes is close to  $1 \mu\text{A}/\text{cm}^2$ . Thus the units of ionic current density in (1) are ( $\mu\text{A}/\mu\text{F}$ ), and a standard cell size is assumed for solutions of the the partial differential equation.

Families of ordinary differential equation cardiac cell models have been developed to describe the voltage and time dependent currents  $I_{\text{ion}}$  [19], that reconstruct the action potential  $V(t)$ . These cell models can be applied hierarchically to construct virtual ventricular tissue models of increasing spatial dimension, with 1-dimensional models for propagation, collision and vulnerability; 2-dimensional models for curvature effects and the initiation, stability and persistence of re-entrant spiral waves, and 3-dimensional models for scroll wave dynamics, and for linking into organ models. The effects of heterogeneities can be explored in 1-, 2- and 3-dimensional models, anisotropy in 2-dimensional models, and rotational anisotropy in 3-dimensional tissue models [26].

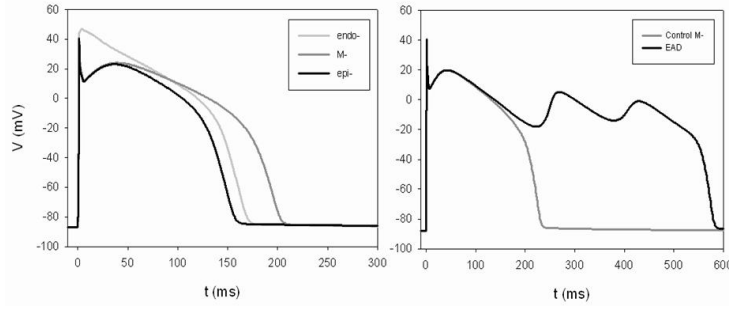


Figure 2. (a) Voltage profiles of single-cell action potentials (APs) for the Luo-Rudy [18] endo-, M- and epicardial cell models, illustrating transmural differences in APD, and (b) for M cells with an EAD induced by a reduced  $G_{K_r}$ .

**Zero-dimensional** ordinary differential equation versions of Eq. 1 (virtual cells) reproduce cell differences between different parts of the heart e.g. the transmural differences illustrated in Fig. 2(a), by having different parameter sets. An increase in these differences, by changes in action potential duration, leading to an increase in the spatial dispersion, due to channel myopathies [27], pathologies [24] or pharmacological actions [28], is arrhythmogenic. Modification of the cell properties can induce pro-arrhythmic early or late afterdepolarisations (Fig. 2(b)) [29]. These cell models can be characterised by their action potentials, thresholds, and their dependence on the timing of previous activity.

**One-dimensional** versions of Eq. (1), with transmural heterogeneities idealise transmural propagation. Similar to the transmural wedge experiments [27] and previous modelling studies [30], our 1D simulations correspond to the situation during the normal heart-beat, where the Purkinje system ensures near-simultaneous excitation of the endocardium, resulting in a planar transmural wavefront parallel to the endocardial surface. The 1D model is sufficient for simulating such a planar wave, its velocity and its nonlinear dispersion (rate dependence).

Transmural differences in the density of two repolarising ionic currents, the slow-delayed rectifier potassium current  $I_{K_s}$  and the transient outward potassium current  $I_{t_o}$ , are introduced to represent three tissue types: endo-, mid-myocardial (M-) and epi-cardial [30]. The density ratio  $I_{K_s}:I_{K_r}$  (here  $I_{K_r}$  is the rapid-delayed rectifier potassium current) is 11:1, 4:1 and 35:1, and maximum conductance of the  $I_{t_o}$  current is 0.0, 0.2125 and 0.25 mS/ $\mu$ F for endo-, M- and epicardial tissue, respectively. For geometric simplicity we assume that each type comprises a uniform region occupying a third of the virtual wall. As the organisation of M-

cells – a laminar, or clustered distribution, and the proportion of endo-, M- and epicardial cells within the wall are not known, this assumption constitutes a first approximation of the transmural cellular structure.

The extracellular potential generated by spatial distributions of the membrane voltage  $V(x, t)$  within the 1D virtual ventricular wall can be approximated by:

$$\Phi_e(x^*, t) = -K \int \frac{\partial V(x, t)}{\partial x} \cdot \frac{\partial}{\partial x} \left( \frac{1}{x^* - x} \right) dx . \quad (2)$$

and related to ECG characteristics [24, 30]. Here  $K$  is a positive constant,  $x^*$  is the distance from epicardial end of the tissue to an in line “electrode” site. The time profile of  $\Phi_e$  constitutes an approximation for the ventricular component of the ECG – a pseudo-ECG.

**Two-dimensional** models are used to simulate initiation of intramural re-entry in slices through the virtual wall. The transmural 1- and 2-dimensional versions of Eq. (1), with zero-flux boundary conditions, were solved numerically using the explicit Euler method with time and space steps  $\Delta t = 0.005$  ms and  $\Delta x = 0.1$  mm. The endocardial edge of the tissue was stimulated by a 0.5 ms,  $-100 \mu\text{A}/\mu\text{F}$  current pulse stimulus (S1), leading to transmural action potential (AP) propagation. The diffusion coefficient is set to a uniform value of  $0.06 \text{ mm}^2/\text{ms}$  through the whole tissue, except for a 5-fold decrease at the boundary between the M-cell and epicardial regions [30], giving a solitary AP propagation velocity of 0.45 m/s and a transmural propagation time of  $\sim 33$  ms. Secondary stimuli (S2) are applied at different test sites through the virtual tissue, and at different time intervals, resulting in either propagation failure, unidirectional propagation block or bidirectional propagation (see Fig. 4). At each spatial point, the vulnerable window (VW) is defined as the range of S2 times within which the unidirectional block is obtained.

**Three-dimensional** versions of Eq. (1) with simplified Fenton-Karma [8] excitation kinetics were solved on the full anisotropic ventricular geometry grid using a finite-difference PDE solver that implements the explicit Euler method with time and space steps  $\Delta t = 0.10$  ms and  $\Delta x = 0.39$  mm.

Ventricular anisotropic geometry has been reconstructed from Diffusion Tensor Imaging. In Diffusion Tensor Magnetic Resonance Imaging a voxel (volume element) averaged diffusion tensor is calculated from the signal attenuation and the intensity of magnetic gradient applied during a diffusion weighted spin-echo experiment [31]. The tensor for each voxel is symmetric, can be represented by the 3 real eigenvalues and the 3 orthogonal eigenvectors, and can be imagined as an ellipsoid, whose axes are orientated along the eigenvectors. The long axis corre-

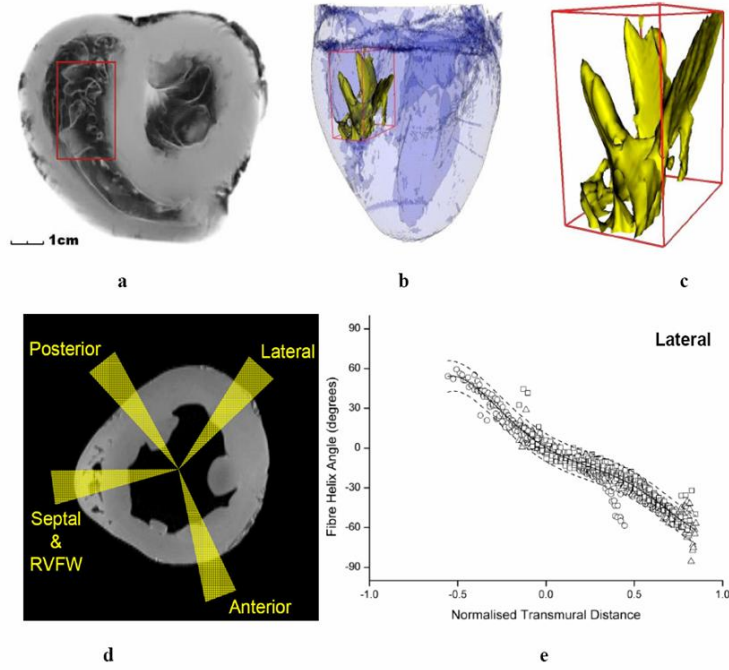


Figure 3. Ventricular geometry reconstructed from an MRI data stack: the spatial resolution is sufficient to identify papillary muscles and their insertions; (a) view into 3D reconstructed ventricle. Unless otherwise specified all subsequent figures use this individual canine cardiac geometry; (b), (c) the 16 by 30 mm rectangles in the right ventricle of (a) are the XY short axis projection of the 16 by 30 by 27 cuboid extracted in (b, c) that illustrate the anterior and posterior papillary muscles. (d) short axis slice through mid ventricle, with (e) transmural fibre orientation through the lateral sectors of three DT-MRI left ventricular free wall

sponds to the direction of greater diffusion that depends on the tissue anisotropy. The primary eigenvector has been validated as a measure of fibre orientation in slabs of ventricular wall [32, 33, 34].

We reconstructed fibre orientation for canine DT-MRI data sets obtained from Ed Hsu at Duke University (the reconstruction method is a whole-ventricle analogue of the method used in [32]) from the primary eigenvectors. The image matrix for the canine ventricular data used here is  $128 \times 128 \times 128$ , representing a physical field of  $100 \times 100 \times 100$  mm, such that each voxel illustrated in Fig. 3 is a cuboid with an approximate side length of  $780 \mu\text{m}$ . This is sufficient to visualise the boundaries of the papillary muscle and their insertions (Fig. 3(c)), which are blurred by temporal averaging in the *in vivo* MRI of the beating heart, and are not apparent in the Auckland canine ventricles.

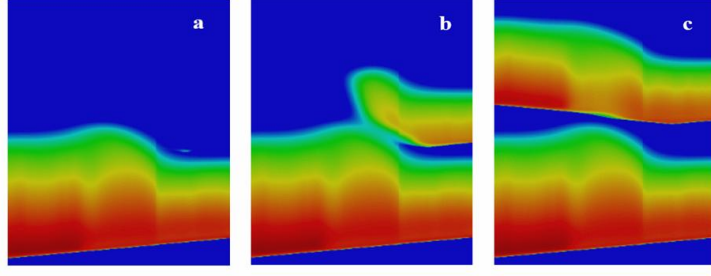


Figure 4. Transmural AP propagation and VW in the Luo-Rudy [18] virtual ventricular wall. The wall is stimulated with an S1 stimulus from the endocardial edge (at the left), leading to an AP propagation. Following S2 stimulation with different timing results in either (a) propagation failure for  $S2 = 160$  ms, (b) unidirectional block for  $S2 = 180$  ms or (c) bidirectional propagation for  $S2 = 200$  ms, where  $S2$  represents the time since the onset of the S1 action potential. Space-time plots are shown, the membrane voltage is colour-coded using the standard rainbow palette. Each panel presents 400 ms of activity in 15 mm thick wall. In this illustration the  $S2$  stimuli are applied in the epicardial region at  $x = 12$  mm.

DT-MRI of isolated hearts provides a high throughput method of reconstruction of detailed, anisotropic ventricular geometry that can be used to construct atlases from a population, to map variability between individuals, as well as to characterise individual geometries.

As cylindrical myocardial cells are aligned parallel to each other, and excitation is conducted more quickly along ventricular fibres than across them [22], we used the values of longitudinal and transverse diffusion coefficients  $D_{\parallel} = 0.2 \text{ mm}^2/\text{ms}$  and  $D_{\perp} = 0.05 \text{ mm}^2/\text{ms}$ , respectively. Ventricular geometry is defined by applying a binary 3D mask to the DT-MRI data, and defining whether a  $780 \mu\text{m}^3$  voxel is inside/outside the ventricles. Fibre orientation is given by the primary eigenvector of the DT-MRI data for each voxel. In order to provide a grid space step sufficiently small for the numerical simulations, the resulting regular Cartesian grid of  $128 \times 128 \times 128$  geometry points with fibre orientation vectors is refined to  $256 \times 256 \times 256$  points. This reduces the distance between the grid points to  $390 \mu\text{m}$ , which is adequate for numerical solutions; the fibre orientation in each of the intermediate points is linearly interpolated.

Linear combinations of the fibre orientation vector with longitudinal and transverse diffusion coefficients  $D_{\parallel}$  and  $D_{\perp}$  give components of the diffusion tensor  $\mathbf{D}$  at each grid point [15].

### 3. Virtual ventricular wall

#### 3.1. CLASS III ANTIARRHYTHMIC ACTIONS

Figure 4 illustrates patterns of action potential propagation through the 1D virtual ventricular wall, produced by endocardial S1 and sub-epicardial S2 stimulations, to illustrate transmural changes in action potential duration, and to define the vulnerable window (VW). Transmural APD profiles and VWs computed for virtual tissues modified to simulate the electrophysiological effects of two Class III drugs – amiodarone and d-sotalol – are shown in Fig. 5. Both amiodarone and d-sotalol are clinically used anti-arrhythmic agents, that as Class III agents act by prolonging action potential duration, *i.e.* delay repolarisation, and both act by decreasing one of the repolarising currents,  $I_{Kr}$ . Clinical trials on patients who already have had a myocardial infarct (damage to heart muscle following a heart attack) has shown that amiodarone has fewer pro-arrhythmic side effects than d-sotalol. The effects of amiodarone and d-sotalol are incorporated in the model as changes in the density of  $I_{Kr}$  ( $\mu A/\mu F$ ) – the primary target for Class III drug action – and the slow L-type calcium current  $I_{Ca,L}$  ( $\mu A/\mu F$ ), which reproduces relative alterations of APD in the three tissue types [35, 36, 37]. For the d-sotalol model  $I_{Kr}$  is depressed by 40% in endo-, by 100% in M-cell and by 65% in the epicardial region; for the amiodarone model  $I_{Kr}$  is uniformly depressed by 50% throughout the wall and  $I_{Ca,L}$  is depressed by 40% in the M-cells.

The shape and extent of the vulnerable windows demonstrates a clear correlation with the respective transmural APD dispersions. As d-sotalol increases the dispersion by a predominant increase of the APD in M-cells, the VW in the endo- and epicardial regions, where unidirectional block persists until the M-cell region is fully repolarised, is wide. Amiodarone, however, decreases the APD dispersion by prolonging action potentials in both endo- and epicardial regions while decreasing action potential duration in the M-cell region. This results in a much narrower APD dispersion and vulnerable window comparable to that of the normal tissue. Pacing the virtual wall at different rates show that the transmural APD dispersion (and hence vulnerability) is larger at low rates, especially with d-sotalol.

We conclude that the relative lack of pro-arrhythmogenic side effects of amiodarone in comparison to other Class III drugs can be explained by its relatively low transmural APD dispersion. This leads to a narrow vulnerable window, and hence, low probability of unidirectional propagation block (which can produce re-entry in 2D, see below) in the virtual tissue. Our simulations also show that in this model APD



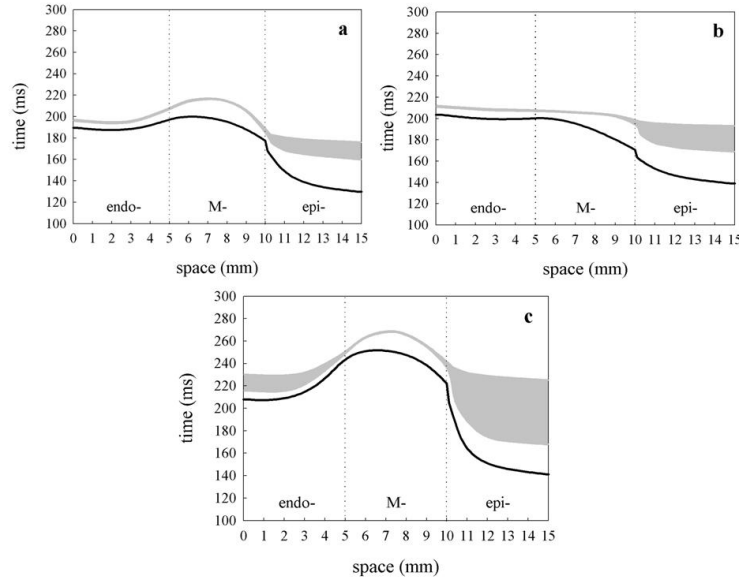


Figure 5. Transmural APD distribution and vulnerability in 1D Luo-Rudy [18] virtual ventricular tissues: (a) normal tissue, (b) with amiodarone, (c) with d-sotalol. Spatial distributions of action potential duration through the tissue (solid lines) are shown along with the respective vulnerable windows (grey areas).

change in M-cells is the major contributor to the transmural APD dispersion, and hence, extent of VW.

### 3.2. EXAMPLE OF RE-ENTRANT ARRHYTHMOGENESIS

We use heterogeneous isotropic 2D virtual tissue to study the effects of transmural APD dispersion on re-entry initiation and the tissue vulnerability to re-entry. Such a tissue idealises a 2D slice through the ventricular wall and, as in 1D case, consists of three regions: endo-, mid-myocardial (M-) and epicardial, each occupying a third of the tissue.

The virtual tissue supports propagating plane waves following S1 stimulation along the endocardial edge. These plane waves have a depolarising wavefront and a repolarising wave back, both aligned parallel to the endocardium. Due to the transmural heterogeneity and differential APDs in epi-, M- and endocardial cells, the repolarisation is non-uniform, and the M-cell region repolarises the last.

In simulations illustrated in Fig. 6, a localised S2 stimulus is applied within the epicardial region of the tissue, where VW is expected to be the widest (see Fig. 5), at different time intervals (S2) following

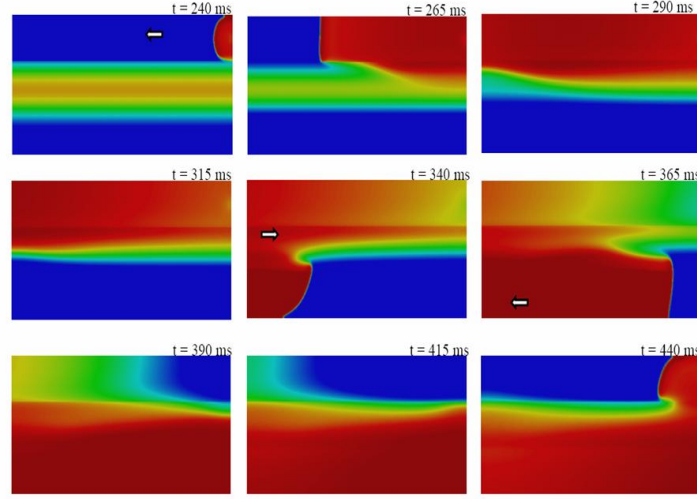


Figure 6. Sustained re-entry in 2D Luo-Rudy [18] virtual ventricular tissue with d-sotalol. Snapshots of the membrane voltage color-coded using the standard rainbow palette are shown at successive moments of time  $t$ . Each panel presents  $15 \times 30 \text{ mm}^2$  tissue composed by endo-, M-cell and epicardial regions,  $5 \times 30 \text{ mm}^2$  each. Initial plane wave propagated from the endocardial (bottom) edge. S2 stimulus is applied at time  $t = 230 \text{ ms}$ .

the onset of the plane wave. When the S2 interval is too short and the epicardial region is still refractory, the stimulus is blocked. When the S2 interval is long enough for the whole tissue to fully repolarise, the stimulus initiates propagation of a circular wave. The vulnerable window in 2-dimensional, heterogeneous tissue is defined as an intermediate range of S2 intervals that produce re-entry, either transient (*i.e.* decaying after a single rotation), or sustained. Sustained re-entry produced by stimulation in the VW and moving around a functional block in the M-cell region is illustrated in Fig. 6. Note that since we use zero-flux boundary conditions, stimulation at the edge of  $15 \times 30 \text{ mm}^2$  tissue corresponds to stimulation in the middle of a symmetric  $15 \times 60 \text{ mm}^2$  tissue. Due to translational symmetry along the horizontal axis, location of the stimulation site along this axis is arbitrary.

Note also that the virtual tissue shown in Fig. 6 is modified with d-sotalol, as sustained re-entry was never observed in the normal tissue or the tissue with amiodarone, where APD in the M-cell region is considerably shorter (see Fig. 5). This is consistent with our electrophysiological explanation for the relative safety of amiodarone in comparison with other Class III antiarrhythmic drugs.

#### 4. Ventricular re-entry and fibrillation

Ventricular fibrillation (VF) is commonly associated with break-up of a single re-entrant scroll wave within the ventricles, and the break-up can be produced by anisotropy of the ventricular wall [8, 15].

We simulate re-entrant scroll waves within the DT-MRI and the Auckland canine ventricular geometries using the simplified Fenton-Karma model [8] for excitation, with parameters to reproduce the Beeler-Reuter ventricular action potential. Re-entry is initiated by stimulating part of the left ventricular wall while maintaining a line of block running from base to apex for 200 ms. Although the detailed geometry of the hearts is quite different, re-entry degenerates into VF after about 400 ms, resulting in irregular spatio-temporal electrical patterns (Fig. 7(b)), and multiplication of filaments (Fig. 7(c, e)) – phase singularities around which re-entrant waves rotate [4, 15]. The electrical activity at any point in the ventricles during VF is an irregular sequence of action potentials and oscillations.

The irregular spatio-temporal surface activity during *in vitro* and simulated VF can be quantified by measures of patterning [12, 38], or by statistics of the number of phase singularities [2, 14, 39] in the ventricular tissue. For 3D simulations, the behavior of filaments during ventricular tachycardia can be quantified by detecting filaments in ventricles from the intersection of  $V = -20$  mV and  $dV/dt = 0$  iso-surfaces, and identified voxels containing filaments [15].

For all the DT-MRI and the Auckland ventricles the number of filaments increases rapidly between about 400 and 800 ms, and then fluctuates around a mean level of about 35 (see Fig. 7(d)). Hence, despite more complex irregular geometry of the endocardium, and irregularities in the fibre orientation vector, DT-MRI ventricles generate fibrillation patterns similar to that seen in the smoothed and histologically derived Auckland ventricles [15, 40].

The breakdown of a re-entrant wave can be due to tissue anisotropy [8], cellular restitution properties [7], or 3D instabilities [9]. Setting the anisotropy ratio  $r = D_{\parallel} / D_{\perp} = 1$  (*i.e.*, removing the effects of anisotropy) resulted in stable rotation of scroll waves in both the DT-MRI and the Auckland ventricles, as predicted in [8]. Interestingly, decreasing the slow inward current by 50% (and hence shortening cellular APD) also stabilised re-entry in both hearts (Fig. 7(e)). The latter result not only shows similar response of the DT-MRI and the Auckland ventricles to cellular changes, but also demonstrates that the breakdown into VF due to tissue anisotropy can be prevented by changing cellular parameters that decrease APD [41].

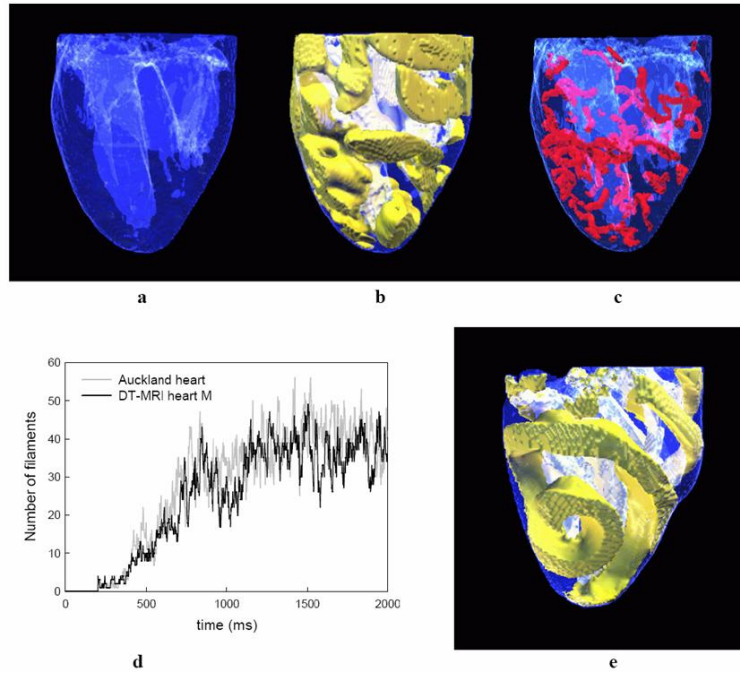


*Figure 7.* Fibrillation in a DT-MRI ventricles. Ventricular geometries (a) are shown along with snap-shots of the membrane potential iso-surfaces  $V = -50$  mV (b) and filaments (c) at time  $t = 2000$  ms after initiation of a broken wavefront. (d) The number of filaments following initiation of re-entry in left ventricle of a DT-MRI heart. Respective statistics of the number of filaments in the Auckland ventricles is shown for comparison in grey line. (e) Re-entrant scroll waves in a DT-MRI ventricles. Snapshots of iso-surfaces of the membrane potential  $V = -50$  mV are shown within the ventricular geometry at time  $t = 2000$  ms after initiation of a broken wavefront with re-entry stabilised by a 50% reduction in the slow inward current. The observation angle has been selected to emphasise the geometry of the scroll wave.

## 5. Summary

Understanding the genesis, development and prevention of cardiac arrhythmias requires direct visualisation of 3 dimensional excitation propagation processes deep within the ventricular walls of a beating, *in vivo* heart. This is not technically feasible, but the virtual ventricular wall, based on detailed single-channel, membrane and cell electrophysiology provides a partially validated means for visualisation, dissecting and explaining propagation in the normal, pathological and pharmacologically modified heart. The one-dimensional virtual ventricular wall has shown that the effects of pathophysiology [24] and pharmacology

(Class III drugs) on the transmural propagation can be explained by changes in the transmural action potential duration (APD) dispersion. The increase/decrease of the tissue vulnerability in response to d-sotalol/amiodarone results from changes in the APD dispersion and the probability of the unidirectional propagation block. We have quantified the role of transmural heterogeneity of virtual ventricular tissue in re-entry initiation, and defined relationships between the transmural APD dispersion and vulnerable properties of the tissue. This allowed us to suggest an electrophysiological explanation for the anti- and proarrhythmic effects of Class III drugs on the transmural propagation: changes in patterns of action potential duration dispersion leading to changes of the global extent of the vulnerable window in the tissue. Thus, the safety of amiodarone in comparison to other Class III drugs can be explained by relatively low transmural APD dispersion leading to a narrow vulnerable window, and hence, a low probability of re-entry in the tissue. Our simulations also show that APD change in mid-myocardial-cells is the major contributor to the transmural APD dispersion, and hence, the tissue vulnerability. Although our models of Class III drug action on the virtual ventricular tissues are geometrically highly simplified, they reproduce relative changes of APD in endocardial, midmyocardial and epicardial tissue, and produce results consistent with a variety of experimental data [35, 36, 37, 42].

The addition of the detailed geometry and anisotropy for an individual heart from magnetic resonance imaging and diffusion tensor magnetic resonance imaging datasets allows the simulation of normal excitation, and abnormal, re-entrant activity during ventricular tachycardia and fibrillation, that can be partially validated by optical monitoring of the surface. All stages of the model construction from the datasets have been automated, to provide a high throughput route to anisotropic virtual ventricles, as a virtual organ source for computational electrophysiology. Although the geometry and fibre orientation of the diffusion tensor reconstructed ventricles is much more complex and irregular than that of the smoothed Auckland ventricles, the filament dynamics in numerical simulations of ventricular fibrillation within these two geometries are quantitatively similar. This provides a validation for individual ventricular geometries constructed based on time-efficient diffusion tensor techniques, and supports the use of diffusion tensor imaging as a high throughput source of cardiac architectures. Our results also show that ventricular fibrillation is robust in respect to spatial irregularities within the ventricles (such as papillary muscles), but can be eliminated by changing cellular restitution properties, primarily by blocking the slow inward membrane current.

## Acknowledgements

This work was supported by the European Union through the Network of Excellence BioSim, Contract No. LHSB-CT-2004-005137, and studentships from the MRC (APB), EPSRC (GH), ORS (PL), and BHF (WCT).

## References

1. Li, D., Li, C.Y., Yong, A.C. & Kilpatrick, D. 1998 Source of electrocardiographic ST changes in subendocardial ischemia. *Circ. Res.* **82**, 957-970.
2. Gray, R.A., Pertsov, A.M. & Jalife, J. 1998 Spatial and temporal organisation during cardiac fibrillation. *Nature* **392**, 75-78.
3. Valderrabano, M., Lee, M.H., Ohara, T., Lai, A.C., Fishbein, M.C., Lin, S.F., Karagueuzian, H.S. & Chen, P.S. 2001 Dynamics of intramural and transmural reentry during ventricular fibrillation in isolated swine ventricles. *Circ. Res.* **88**, 839-848.
4. Gray, R.A., Jalife, J., Panfilov, A.V., Baxter, W.T., Cabo, C., Davidenko, J. M. & Pertsov, A.M. 1995 Mechanisms of Cardiac Fibrillation. *Science* **270**, 1222-1223.
5. Panfilov, A. & Pertsov, A.M. 2001 Ventricular fibrillation: evolution of the multiple-wavelet hypothesis, *Phil. Trans. Royal Soc. Lond. A - Math. Phys. Eng. Sci.* **359**, 1315-1325.
6. Zaitsev, V., Berenfeld, O., Mironov, S.F., Jalife, J. & Pertsov, A.M. 2000 Distribution of excitation frequencies on the epicardial and endocardial surfaces of fibrillating ventricular wall of the sheep heart. *Circ. Res.* **86**, 408-417.
7. Garfinkel, A., Kim, Y.H., Voroshilovsky, O., Qu, Z.L., Kil, J.R., Lee, M.H., Karagueuzian, H.S., Weiss, J.N. & Chen, P.S. 2000 Preventing ventricular fibrillation by flattening cardiac restitution. *Proc. Nat. Acad. Sci. USA* **97**, 6061-6066.
8. Fenton, F.H. & Karma, A. 1998 Vortex dynamics in three-dimensional continuous myocardium with fibre rotation: Filament instability and fibrillation. *Chaos* **8**, 20-47.
9. Biktashev, V.N., Holden, A.V. & Zhang, H. 1994 Tension of organizing filaments of scroll waves. *Phil. Trans. R. Soc. Lond. A* **347**, 611-630.
10. Janse, M.J., Van-Cappelle, F.J.L., Morsink, H., Kleber, A.G., Wilms-Schopman, F., Cardinal, R., D'Almoncourt, C.N. & Durrer, D. 1980 Flow of "injury" currents and patterns of excitation during early ventricular arrhythmias in acute regional myocardial ischaemia in isolated porcine and canine hearts. Evidence for two different arrhythmogenic mechanisms. *Circ. Res.* **47**, 151-165.
11. Ideker, R.E., Klein, G.J., Harrison, L., Smith, W.M., Kasell, J., Reimer, K.A., Wallace, A.G. & Gallagher, J.J. 1981 The transition to ventricular fibrillation induced by reperfusion after acute regional ischaemia in the dog: A period of organised epicardial activation. *Circulation* **63**, 1371-1379.
12. Biktashev, V.N., Holden, A.V., Mironov, S.F., Pertsov, A.M. & Zaitsev, A.V. 1999 Three-dimensional aspects of re-entry in experimental and numerical models of ventricular fibrillation. *Int. J. Bifurcat. & Chaos* **9**, 695-704.

13. Kay, M.W., Amison, P.M. & Rogers, J.M. 2004 Three-dimensional surface reconstruction and panoramic optical mapping of large hearts. *IEEE Trans. Biomed. Eng.* **51**, 1219-1229.
14. Rogers, J.M. 2004 Combined phase singularity and wavefront analysis for optical maps of ventricular fibrillation. *IEEE Trans. Biomed. Eng.* **51**, 56-65.
15. Clayton, R.H. & Holden, A.V. 2004 Filament behavior in a computational model of ventricular fibrillation in the canine heart. *IEEE Trans. Biomed. Eng.* **51**, 28-34.
16. Clayton, R.H. & Holden, A.V. 2005 Dispersion of cardiac action potential duration and the initiation of re-entry: A computational study. *Biomed. Eng. Online* **4**, 11-16.
17. Xie, F., Qu, Z., Yang, J., Baher, A., Weiss, J.N. & Garfinkel, A. 2004 A simulation study of the effects of cardiac anatomy in ventricular fibrillation. *J. Clin. Invest.* **113**, 686-693.
18. Luo, C.H. & Rudy Y. 1994 A dynamic model of the cardiac ventricular action potential. I. Simulations of ionic currents and concentration changes. *Circ. Res.* **74**, 1071-1096.
19. Noble, D. & Rudy, Y. 2001 Models of cardiac ventricular action potentials: iterative interaction between experiment and simulation. *Phil. Trans. Royal Soc. Lond. A - Math. Phys. Eng. Sci.* **359**, 1127-1142.
20. Boyett, M.R., Jue Li, Inada, S., Dobrzynski, H., Schneider, J.E., Holden, A.V., Zhang, H. Imaging the heart: computer 3-dimensional anatomic models of the heart. *J. of Electrocardiology* **38** 113-120 S
21. LeGrice, I.J., Hunter, P.J. & Smaill, B.H. 1997 Laminar structure of the heart: ventricular myocyte arrangement and connective tissue architecture in the dog. *Am. J. Physiol. - Heart Circ. Physiol.* **269**, H571-H582.
22. Nielson, P.M.F., LeGrice, I.J., Smaill, B.H. & Hunter, P.J. 1991 Mathematical model of the geometry and fibrous structure of the heart. *Am. J. Physiol. - Heart Circ. Physiol.* **260**, H1365-H1378.
23. Kohl, P., Noble, D., Winslow, R.L. & Hunter, P.J. 2000 Computational modelling of biological systems: tools and visions. *Phil. Trans. R. Soc. A* **358**, 579-610.
24. Aslanidi, O.V., Clayton, R.H., Lambert, J.L. & Holden, A.V. 2005 Dynamical and cellular electrophysiological mechanisms of ECG changes during ischaemia. *J. Theor. Biol.* **237**, 369-381
25. Jack, J.J.B., Noble, D. & Tsien, R.W. 1975 *Electric Current Flow in Excitable Cells*. Oxford: Clarendon Press.
26. Panfilov, A.V. & Holden, A.V. 1997 *Computational Biology of the Heart*. Wiley: Chichester.
27. Antzelevitch, C., Yan, G.X. & Shimizu, W. 1999 Transmural dispersion of repolarization and arrhythmogenicity: the Brugada syndrome versus the long QT syndrome. *J. Electrocardiol.* **32**, 158-165.
28. Aslanidi OV, Bailey A, Biktashev VN Holden, A.V. 2002. Enhanced self-termination of re-entrant arrhythmias as a pharmacological strategy for antiarrhythmic action *Chaos* **12**, 843-851
29. Viswanathan, P.C. and Rudy, Y. 2000. Cellular Arrhythmogenic Effects of Congenital and Acquired Long-QT Syndrome in the Heterogeneous Myocardium. *Circulation* **101**, 1192 - 1198.
30. Gima, K. & Rudy, Y. 2002 Ionic current basis of electrocardiographic waveforms – a model study. *Circ. Res.* **90**, 889-896.

31. Basser, P.J., Mattiello, J. & LeBihan, D. 1994 Estimation of the effective self-diffusion tensor from the NMR spin echo. *J. Magnet. Res. Med.* **30**, 201-206.
32. Hsu, E.W., Muzikant, A.L., Matulevicius, S.A., Penland, R.C. & Henriquez, S.C. 1998 Magnetic resonance myocardial fiber-orientation mapping with direct histological correlation. *Am. J. Physiol. - Heart Circ. Physiol.* **274**, H1627-H1634.
33. Holmes, A.A., Scollan, D.F. & Winslow, R.L. 2000 Direct histological validation of diffusion tensor MRI in formaldehyde-fixed myocardium. *J. Magnet. Res. Med.* **44**, 157-161.
34. Scollan, D.F., Holmes, A., Winslow, R.L. & Forder, J. 1998 Histological validation of myocardial microstructure obtained from diffusion tensor magnetic resonance imaging. *Am. J. Physiol. - Heart Circ. Physiol.* **275**, H2308-H2318.
35. Sicouri, S., Moro, S., Litovsky, S., Elizari, M.V. & Antzelevitch, C. 1997 Chronic amiodarone reduces transmural dispersion of repolarization in the canine heart. *J. Cardiovasc. Electrophysiol.* **8**, 1269-1279.
36. Akar, F.G., Yan, G.-X., Antzelevitch, C. & Rosenbaum, D.S. 2002 Unique topographical distribution of M cells underlies re-entrant mechanism of Torsade de Pointes in the Long-QT syndrome. *Circulation* **105**, 1247-1253.
37. Drouin, E., Lande, G. & Charpentier, F. 1998 Amiodarone reduces transmural heterogeneity of repolarization in the human heart. *J. Am. Coll. Cardiol.* **32**, 1063-1067.
38. Biktashev, V.N. & Holden, A.V. 2001 Characterization of patterned irregularity in locally interacting, spatially extended systems: Ventricular fibrillation. *Chaos* **11**, 653-664.
39. Witkowski, F.X., Leon, L.J., Penkoske, P.A., Clark, R.B., Spano, M.L., Ditto, W.L. & Giles, W.R. 1998. A method for visualization of ventricular fibrillation: Design of a cooled fiber optically coupled image intensified CCD data acquisition system incorporating wavelet shrinkage based adaptive filtering. *Chaos* **8**, 94-102.
40. Panfilov, A. 1999 Three-dimensional organization of electrical turbulence in the heart. *Phys. Rev E* **59**, R6251-R6254.
41. Weiss, J.N., Chen, P-S, Qu, Z., Karagueuzian, H.S., Garrfinkel, A. 2000. Ventricular fibrillation – How do we stop the waves from breaking? *Circulation Research* **87**, 1103-1107.
42. Huikuri, H.V., Castellanos, A. & Myerburg, R.J. 2001 Sudden death due to cardiac arrhythmias. *N. Engl. J. Med.* **345**, 1473-1482.